HOKKAIDO UNIVERSITY

Title	Skull shape differences among Myanmar and adjacent populations of the house shrew, Suncus murinus (Mammalia: Eulipotyphla): Insights into allometry and phylogenetic variances using geometric morphometrics
Author(s)	Ikeda, Yugo; Yamagata, Takahiro; Bawm, Saw et al.
Citation	Mammal study, 50(1), 27-38 https://doi.org/10.3106/ms2023-0071
Issue Date	2024-09-10
Doc URL	https://hdl.handle.net/2115/97500
Type	journal article
File Information	MS2023-0071.R4_Proof_fl.pdf

Hokkaido University Collection of Scholarly and Academic Papers : HUSCAP

Skull shape differences among Myanmar and adjacent populations of the house shrew, *Suncus murinus* (Mammalia: Eulipotyphla): Insights into allometry and phylogenetic variances using geometric morphometrics

Yugo Ikeda [1,2 *], Takahiro Yamagata [3], Saw Bawm [4], Thidalay Thwe [5], Khin Myat Myat Zaw [5], Masaharu Motokawa [1] and Satoshi D. Ohdachi [6]

[1] *Kyoto University Museum, Kyoto University, Yoshida-honmachi, Sakyo, Kyoto 606-8501, Japan.*

[2] *Graduate School of Agricultural and Life Sciences, The University of Tokyo, Tokyo 113-8657, Japan.*

[3] *Laboratory of Animal Genetics and Breeding, Graduate School of Bioagricultural Sciences, Nagoya University, Furo-Cho, Chikusa, Nagoya 464-8601, Japan.*

[4] *Department of Livestock and Aquaculture Research, Nay Pyi Taw, 15013, Myanmar.*

[5] *Department of Zoology, Yangon University of Distance Education, Yangon, 11041, Myanmar.*

[6] *Institute of Low Temperature Science, Hokkaido University, Kita-ku, Sapporo 060-0819, Japan.*

[*] *To whom correspondence should be addressed: j.dranimal@gmail.com*

Abstract. In Southeast and South Asia including Myanmar and Bangladesh, the house shrew (*Suncus murinus*) is widely distributed and consists of multiple lineages based on mitochondrial DNA. However, there has been no morphometric investigation among such lineages, despite the obvious recognition of large variation in their body size and shape geographically. To elucidate morphological differences among local populations in reference to multiple lineages of *S. murinus*, we conducted geometric morphometrics to investigate skull morphological variations focusing on highly diverged Myanmar and adjacent Bangladesh and Vietnam populations. Our findings indicate that skull shape changes can distinguish adjacent lineages, and some

individuals represent intermediate forms between the two geographically adjacent lineages. The results also represent several overlaps of skull size and allometric shape changes among Myanmar populations, suggesting the presence of intermediate individuals due to hybridization. Additionally, allometric shape changes were observed in the sites of attachment of muscles or tendons between the cranium and the mandible suggesting an association with piecing or decaying. Our findings provide fundamental insights into the skull morphological features of *S. murinus*, that contributes to a more comprehensive understanding of the evolutionary processes of morphological variation in the house shrew.

Key words: phylogeography, geographic variation, hybridization, Musk shrew, skull morphology.

The Asian house shrew, *Suncus murinus* (Linnaeus 1766) (Eulipotyphla, Soricidae, Crocidurinae) is originally distributed throughout the Indo-Malayan Region and southern China, including Taiwan, Hainan, and Sri Lanka (Burgin and He 2018). *Suncus murinus* was introduced in historical times into Maldives, islands of Malaysia, Indonesia, Brunei, Philippines, Japan (Kyushu and Ryukyu Is.), Guam, Palau, and New Guinea, East Africa, Pemba and Zanzibar Is., Madagascar, Comoro Is., Mauritius, Reunion Is., and the coastal region of Arabia (Hutterer 2005; Motokawa 2015; Burgin and He 2018; Ohdachi et al. 2024). Previous molecular phylogenetic studies have provided valuable insights into the origin and evolutionary history of *S. murinus*. Clustering analysis of mitochondrial DNA haplotypes has classified them into two lineages: Southeast Asia and the South Asian continent (Yamagata et al. 1995; Yamagata 2011). Further phylogenetic trees based on the mitochondrial cytochrome *b* gene revealed four independent lineages (Ohdachi et al. 2016, 2024), and one of the lineages (Lineage I) likely spread throughout the tropical or subtropical

regions in East, Southeast, and South Asia, and coastal islands around Indian Ocean toward Madagascar, involving transportation with humans via trade ships (Yoshida 1982; Hutterer and Trainier 1990; Yamagata et al. 1995; Kurachi et al. 2007a, 2007b; Ohdachi 2021; Ohdachi et al. 2024). Interestingly, *S. murinus* from Myanmar showed high divergence, splitting into three lineages: southern (Lineage I), central (Lineage II), and western Myanmar (Lineage III, Ohdachi et al. 2017; Ohdachi 2021; Ohdachi et al. 2024).

While previous studies have revealed genetic differences among local populations of *S. murinus*, their morphological distinctions have remained unclear. *Suncus murinus* exhibits extensive morphological variation in body size both geographically and individually (Burgin and He 2018), and also under laboratory conditions (Oda and Kondo 1976; Ishikawa and Namikawa 1991; Ebukuro 2011). For instance, the breeding strain of *S. murinus* from Mymensingh, Bangladesh (BAN strain), is significantly larger than other strains, whereas the stock from Nagasaki, Japan (NAG

strain), is smaller (Ishikawa and Namikawa 1987). The F_1 and F_2 generations of hybrid progeny resulting from a cross between BAN and NAG strains showed an intermediate body size compared to the two strains, and the body size of *S. murinus* is indicated to be under polygenic control (Ishikawa and Namikawa 1991).

Due to the high variation in their body size, understanding allometry is essential to reveal morphological distinctions of *S. murinus*. The mammalian skull is generally known to change shape and/or proportion in correlation with body size (Emerson and Bramble 1993; Marroig et al. 2009). According to Ishikawa et al. (1995), the skull size of *S. murinus* is concordant with the phylogenetic pattern indicated by Yamagata et al. (1995), in addition to body size; however, the skull shape is not entirely concordant. The variations in skull shape are not always due to allometry; they also encompass non-allometric shape changes. However, there is no study that comprehensively addresses the allometric and non-allometric shape changes in the skull of *S. murinus*.

To explore the morphological shape variations among lineages, size-adjusted

morphometric methods, such as geometric morphometrics, are effective, allowing the comprehensive understanding of both allometry and non-allometry (Klingenberg 2016).

This study aimed to explore the differences in skull shape among highly diverged populations of *S. murinus* in Myanmar, along with the adjacent populations in Bangladesh and Vietnam, by elucidating allometric and non-allometric shape changes in the skull using geometric morphometrics.

Materials and methods

Specimens and sampling localities

We analyzed a total of 127 skull specimens of adjacent *S. murinus* populations collected from highly diverged regions: Bangladesh (ten males and 12 females), western Myanmar (W. Myanmar, three males and five females), central Myanmar (C. Myanmar, six males and five females), southern Myanmar (S. Myanmar, 22 males and

27 females), and Vietnam (19 males and 18 females, Table 1). The geographical distribution of the sampling localities is shown in Fig. 1. Detailed information on the locality, specimen name, sex, and collected date for each individual is available at the following link:

https://www.google.com/maps/d/edit?mid=1JvPgDIEzyaMAQHqGWVmcPLEPCbijRWo&usp=sharing.

Landmarking

For this study, we employed the geometric morphometric method. Ventral and right lateral aspects of the cranium, as well as the mandible from the right lateral aspect, were photographed for each specimen using an EOS Kiss X8i camera and EF 100 mm F 2.8 Macro USM lens, Canon, with a resolution of 6000 × 4000 pixels. All images were taken at a constant angle, following the approach by Ikeda et al. (2020). We identified 30 landmarks on the ventral aspect of the cranium, 22 landmarks (including eight semi-landmarks) on the lateral aspect of the cranium, and ten landmarks on the

lateral aspect of the mandible (Fig. 2). These landmarks were digitized using tpsDIG2 software (Rohlf 2017). Definitions of each landmark are provided in Table S1. All skull images were then converted to tps format using the tps Utility program (Rohlf 2018). The analysis included 127 specimens (60 males and 67 females) with complete sets of landmarks on the ventral aspect of the cranium, 125 specimens (59 males and 66 females) on the lateral aspect of the cranium, and 122 specimens (57 males and 65 females) on the lateral aspect of the mandible.

Morphometric analyses

To extract skull shape variation while eliminating differences due to displacement, rotation, and scaling (Rohlf and Slice 1990), we conducted a Generalized Procrustes Analysis (GPA; Bookstein 1991). Centroid size (CS) was calculated for each specimen as the square root of the sum of the squared Euclidean distances of each landmark to the mass center of each configuration. Initially, a linear correlation between Log-transformed centroid size (logCS) and body weight was analyzed to confirm that CS

functioned as the size variable. Subsequently, logCS was used as the size valuable, and Procrustes coordinates were used as the shape valuable. A two-way (sex × locality) analysis of variance (ANOVA) and multivariate analysis of variance (MANOVA) were performed on logCS and Procrustes coordinates, respectively. For statistical analyses, we used R package "Geomorph" version 4.0.6 (Baken et al. 2021; Adams et al. 2023; Collyer and Adams 2023) with R software version 4.2.2 (R Development Core Team 2022).

Next, to extract the skull allometric shape change from the overall shape change, we conducted a regression analysis for logCS correction of the shape data, following the approach by Klingenberg (2016). Afterward, we performed size-adjusted Canonical Variate Analysis (CVA) on the residuals of the regression. For the CVA, we considered five localities (Bangladesh, W. Myanmar, C. Myanmar, S. Myanmar, and Vietnam) as a group to detect geographic skull shape variation. The regression analysis was performed using R package "Geomorph" version 4.0.6 (Baken et al.

2021; Collyer and Adams 2023; Adams et al. 2023) with R software version 4.2.2 (R Development Core Team 2022), and size-adjusted CVA was performed using MorphoJ version 1.07a (Klingenberg 2011).

Results

A linear correlation between two size variables

A linear correlation analysis between logCS body weight revealed a significant correlation for both aspects of the cranium ($t_{122} = 26.49$, $P < 0.001$ for the ventral aspect; $t_{120} = 23.87$, $P < 0.001$ for lateral aspect) as well as for the mandible ($t_{117} = 21.55$, $P < 0.001$). The Pearson correlation coefficient I was calculated for both aspects of the cranium ($r = 0.923$ for the ventral aspect; $r = 0.909$ for the lateral aspect) and the mandible ($r = 0.894$, see also Appendix 1). Specimens with missing values in body weight or logCS were excluded from the analysis.

The variations among size and shape variables

A two-way (sex × locality) ANOVA of logCS revealed significant size differences among sexes for both aspects of the cranium ($F_{1,126} = 87.586$, $P < 0.001$ for the ventral aspect; $F_{1,124} = 77.374$, $P < 0.001$ for the lateral aspect) and the mandible ($F_{1,121} = 60.098$, $P < 0.001$). Additionally, significant size differences were observed among localities for both aspects of the cranium ($F_{4,123} = 89.835$, $P < 0.001$ for the ventral aspect; $F_{4,121} = 88.787$, $P < 0.001$ for the lateral aspect) and the mandible ($F_{4,118} = 68.113$, $P < 0.001$). No significant interaction between sex and locality was observed on logCS for the ventral aspect of the cranium ($F_{4,123} = 1.362$, $P = 0.261$) and the mandible ($F_{4,118} = 0.695$, $P = 0.579$), but significant interaction was observed for the lateral aspect of the cranium ($F_{4,121} = 3.494$, $P = 0.017$).

Similarly, a two-way (sex × locality) MANOVA of Procrustes coordinates revealed significant shape differences among sexes for both aspects of the cranium ($F_{1,126} = 8.096$, $P < 0.001$ for the ventral aspect; $F_{1,124} = 13.409$, $P < 0.001$ for the lateral aspect) and the mandible ($F_{1,121} = 7.791$, $P < 0.001$). Additionally, significant shape

differences were observed among localities for both aspects of the cranium ($F_{4,123}$ = 5.485, $P < 0.001$ for the ventral aspect; $F_{4,121} = 5.056$, $P < 0.001$ for the lateral aspect) and the mandible ($F_{4,118} = 7.100$, $P < 0.001$). No significant interaction between sex and locality was observed on Procrustes coordinates for both aspects of the cranium ($F_{4,123} = 0.618$, $P = 0.987$ for the ventral aspect; $F_{4,121} = 1.383$, $P = 0.093$ for the lateral aspect) and the mandible ($F_{4,118} = 1.021$, $p = 0.406$).

The skull shape change related to size

The skull allometric shape change related to logCS was extracted from the overall shape change as regression scores (Fig. 3, vertical axis). A two-way (sex × locality) ANOVA of the regression scores revealed significant size differences among sexes for both aspects of the cranium ($F_{1,126} = 49.301$, $P < 0.001$ for the ventral aspect; $F_{1,124}$ = 50.762, $P < 0.001$ for the lateral aspect) and the mandible ($F_{1,121} = 11.790$, $P = 0.002$). Additionally, significant size differences were observed among localities for both aspects of the cranium ($F_{4,123} = 34.860$, $P < 0.001$ for the ventral aspect; $F_{4,121} = 7.858$,

$P < 0.001$ for the lateral aspect) and the mandible ($F_{4,118} = 8.550$, $P < 0.001$). No significant interaction between sex and locality was observed on regression scores for the ventral aspect of the cranium ($F_{4,123} = 1.206$, $P = 0.326$) and the mandible ($F_{4,118} = 2.106$, $P = 0.082$), but significant for the lateral aspect of the cranium ($F_{4,121} = 2.612$, $P = 0.035$). The boxplots of logCS and regression scores for each aspect of the cranium and the mandible, along with the results of Tukey's Honestly Significant Difference (Tukey HSD), are presented in Fig. 4.

The transformation grid illustrates the shape change along with landmarks based on regression scores. For the ventral aspect of the cranium, the transformation grids of regression scores showed large vector values for landmarks 2–3, 10–15, 17–20, and 23–24 (Figs. 2A and 3A). Positive regression scores indicated four cranial shape trends among larger specimens: the base of the first incisor is wider (landmarks 2–3); the lateral projection of the maxilla is located anteriorly (landmark 10–13), and the choana is narrower (landmarks 14–15); the glenoid fossa is more developed (landmarks 17–

20); and the basilar part of the occipital bone is located posteriorly (landmarks 23–24).

For the lateral aspect of the cranium, the transformation grids of regression scores represented large vector values for landmarks 3, 5, 8–11, and 14–17 (Figs. 2B and 3B). Positive regression scores indicated four cranial shape trends among specimens: the lateral projection of the maxilla is located anteriorly downward (landmark 3); the pterygoid hamulus is located anteriorly (landmark 5); the base of the occiput, consisting of the posterior temporalis crest, the petrous part of the temporal bone, and the occipital condyle, is located upward (landmarks 8–11); and the posterior external sagittal crest and the external occipital protuberance are located posteriorly downward (landmarks 14–17). For the lateral aspect of the mandible, the transformation grids of regression scores represented large vector values for landmarks 1–3, and 9 (Figs. 2C and 3C). Positive regression scores indicated two mandibular shape trends among specimens: the base of the first incisor is shortened and thickened (landmarks 1–3);

and the superior crest of the coronoid process is elongated (landmark 9). The residuals of the regression analysis were used in further size-adjusted analysis.

The non-allometric skull shape variation among localities

The size-adjusted CVA was performed on the residuals of the regression analysis, resulting in four canonical variates (CV) computed for each aspect of the skull. Due to a two-way (sex × locality) MANOVA of residuals revealed no significant differences among sexes for both aspects of the cranium ($F_{1,126}$ = 1.604, P = 0.082 for the ventral aspect; $F_{1,124}$ = 1.005, P = 0.403 for the lateral aspect) and the mandible ($F_{1,121}$ = 1.104, P = 0.324), we treated males and females together. Scatter plots, the contribution ratio of CVs, and transformation grids of shape change were represented in Fig. 5 (CV1 and CV2) and Fig. 6 (CV3 and CV4). For all aspects of the skull, CV1 represented the different shapes between Vietnam and S. Myanmar. Both aspects of the cranium, CV2 represented the different shapes between S. Myanmar and C. Myanmar, and CV3 represented the different shapes between W. Myanmar and other

groups. CV4 represented overlap among groups, and W. Myanmar showed large variance.

The transformation grid illustrates the shape change along with landmarks based on CVs. For the ventral aspect of the cranium, the transformation grids of CV1 represented large vector values for landmarks 1, 16, 19–20, 21–22, and 25–26 (Fig. 5A, horizontal axis). Positive CV scores indicated four cranial shape trends among specimens: the palate is shortened (landmarks 1 and 16); the glenoid fossa develops inward (landmarks 19–20); the tympanic cavity space expands anteriorly (landmarks 21–22); and the mastoid process is located posteriorly (landmarks 25–26). For the ventral aspect of the cranium, the transformation grids of CV2 represented large vector values for landmarks 2–3, 10–13, 21–24, and 27 (Fig. 5A, vertical axis). Positive CV scores indicated four cranial shape trends among specimens: the base of the first incisor is located posteriorly (landmarks 2–3); the lateral projection of the maxilla is located anteriorly and narrower (landmarks 10–13); the tympanic cavity space shrinks

235 posteriorly (landmarks 21–22); and the basilar part of the occipital bone is shorter (landmarks 23–24, 27). For the ventral aspect of the cranium, the transformation grids of CV3 represented large vector values for landmarks 14–16, 17–18, and 27 (Fig. 6A, horizontal axis). Positive CV scores indicated three cranial shape trends among specimens: the posterior part of the palate is located anteriorly (landmarks 14–16); the 240 glenoid fossa is located anteriorly inward (landmarks 17–18); and the foramen magnum is located posteriorly (landmark 27). For the ventral aspect of the cranium, the transformation grids of CV4 represented large vector values for landmarks 5–16, 19–20, and 28–29 (Fig. 6A, vertical axis). Positive CV scores indicated two cranial shape trends among specimens: the palate is larger and pointed (landmarks 5–16); the 245 proximal margin of the glenoid fossa is located anteriorly (landmarks 10–15); and the occipital condyle is wider (landmarks 28–29).

The transformation grids of CV1 of the lateral aspect of the cranium represented large vector values for landmarks 2, 6–11, 13, and 15–16 (Fig. 5B, horizontal axis).

Positive CV scores indicated four cranial shape trends among specimens: the base of the anterior part of the cranium is located posteriorly (landmarks 2, 6–7); the base of the posterior part of the cranium is located anteriorly (landmarks 8–10); the occipital condyle is located lower (landmarks 11 and 13); and the posterior part of the sagittal crest develops (landmarks 15–16). The transformation grids of CV2 of the lateral aspect of the cranium represented large vector values for landmarks 1, 3, 6, 8, 14, 16–17, and 22 (Fig. 5B, vertical axis). Positive CV scores indicated four cranial shape trends among specimens: the first incisor is located lower (landmarks 1 and 22); the maxilla and the pterygopalatine fossa is located anteriorly upper (landmarks 3 and 6); the posterior temporalis crest is located anteriorly upper (landmark 8); and the external occipital protuberance is located posteriorly upper, and the sagittal crest is vulnerable (landmarks 14, 16–17). The transformation grids of CV3 of the lateral aspect of the cranium represented large vector values for landmarks 6–7, 9–10, and 14–15 (Fig. 6B, horizontal axis). Positive CV scores indicated three cranial shape trends among

specimens: the orbitotemporal fossa leans forward (landmarks 6–7); the petrous part of the temporal bone is located posteriorly (landmarks 9–10); and the external occipital protuberance is located anteriorly (landmarks14–15). The transformation grids of CV4 of the lateral aspect of the cranium represented large vector values for landmarks 1, 3–4, 6, 8–10, and 14–17 (Fig. 6B, vertical axis). Positive CV scores indicated four cranial shape trends among specimens: the first incisor is located anteriorly (landmark 1); the maxilla and the pterygopalatine fossa are located posteriorly (landmarks 3–4, 6); the tympanic cavity is located posteriorly, and the occipital condyle is smaller (landmarks 8–10); and the sagittal crest is located anteriorly (landmarks 14–17).

The transformation grids of CV1 of the lateral aspect of the mandible represented large vector values for landmarks 3–4 and 8–10 (Fig. 5C, horizontal axis). Positive CV scores indicated two mandibular shape trends among specimens: the body of the mandible is thick, and the angular process develops (landmarks 3–4); the fossa masseterica expands (landmarks 8–10). The transformation grids of CV2 of the lateral

aspect of the mandible represented large vector values for landmarks 3–4 and 10 (Fig. 5C, vertical axis). Positive CV scores indicated three mandibular shape trends among specimens: the curve of the body of the mandible is mild (landmark 3); the angular process is thinner (landmark 4); the junction of the ramus is deeper (landmark 10). The transformation grids of CV3 of the lateral aspect of the mandible represented large vector values for landmarks 3 and 5–6 (Fig. 6C, horizontal axis). Positive CV scores indicated two mandibular shape trends among specimens: the body of the mandible is narrower (landmark 3); and the angular process elongates (landmarks 5–6). The transformation grids of CV4 of the lateral aspect of the mandible represented large vector values for landmarks 3–4 and 9–10 (Fig. 6C, vertical axis). Positive CV scores indicated three mandibular shape trends among specimens: the body of the mandible is narrower (landmarks 3–4); the end of the superior crest of the coronoid process is located posteriorly (landmark 9); and the fossa masseterica is thinner (landmarks 9–10).

Discussion

Skull morphological differences among geographically adjacent lineages

Although it is necessary to note the small sample size for western Myanmar (three males and five females) and central Myanmar (six males and five females) in this study, our results revealed differences in skull morphology of *S. murinus* among five local populations from Bangladesh, Myanmar, and Vietnam. These skull morphological differences were separated into two features: differences in skull size (logCS) and allometric shape, and differences in non-allometric shape. The five local populations from Myanmar, Bangladesh, and Vietnam could be broadly distinguished into three based on logCS: Bangladesh and western Myanmar represented larger logCS, central Myanmar represented medium logCS, and southern Myanmar and Vietnam represented smaller logCS (Figs. 3 and 4). This split was concordant with molecular phylogenetic results (Ohdachi et al. 2024). Alongside logCS, allometric

shape variations at the sites of attachment of muscles and tendons on the skull indicated from regression scores (Fig. 3), further highlighting differences among populations. These size-related differences also included individuals exhibiting intermediate features. Additionally, the results of size-adjusted CVA provide valuable insights into the skull shape variation of *S. murinus* between Vietnam and southern Myanmar (Fig. 5; CV1), central Myanmar (Fig. 5; CV2), and western Myanmar (Fig. 6; CV3): Vietnam is distinguished by the proximal shift, and southern Myanmar by the distal shift of the base of the cranium with the pterygoid hamulus as the axis; central Myanmar by the posteriorly lower shift of the maxilla; western Myanmar by the extroversion of the glenoid cavity.

Causes of the occurrence of intermediate individuals

While size-adjusted CVA represented clear skull shape differences among lineages, logCS and regression scores showed several overlaps among Myanmar populations. Our results revealed the presence of several individuals with intermediate size, both in

body weight and logCS, among central Myanmar and adjacent southern Myanmar populations (Appendix 1). The overlaps between logCS and regression scores among adjacent populations in Myanmar further support the intermediation (Fig. 3). Among several possibilities as causes for the intermediation in size and allometric shape changes, hybridization suggested by Ishikawa and Namikawa (1991) under experimental conditions may be the most plausible. The western, central, and southern Myanmar populations are phylogenetically differentiated but geographically adjacent. Assuming hybridization among Myanmar populations, it is predicted that intermediate individuals might occur between these populations. In addition to hybridization, it might be necessary to consider the effect of latitude and sexual dimorphism on size and allometric shape changes. In mammals, individuals from higher latitudes usually represent larger body size, as known as Bergmann's rule (Bergmann 1847; Blackburn et al. 1999). However, according to Ishikawa and Namikawa (1987), the body size of the Nagasaki population, located at a higher latitude than Bangladesh, represents a

much smaller body size. The Nagasaki population belongs to the same lineage as the Vietnam population and is considered to have been artificially introduced. Therefore, it is more likely to reflect the morphological characteristics of the original population rather than environmental factors such as latitude (e.g., Ohdachi et al. 2024). This may explain why it does not conform to Bergmann's rule. Additionally, the global test (two-way ANOVA) of size variables conducted in this study revealed significant differences not only among localities but also between males and females. The values were found to be significantly larger in males from Bangladesh and western Myanmar, while smaller in females from southern Myanmar and Vietnam. The Tukey HSD results shown by the combinations of lowercase alphabets in Fig. 4 indicated that relatively large females in Bangladesh and western Myanmar often overlap with relatively small males in southern Myanmar and Vietnam. This sexual dimorphism in body size is expected to emphasize morphological differences in the genital organs between males and females, which may induce reproductive isolation. Specifically,

this implies that while hybridization may occur between larger females and smaller males, it may not occur between smaller females and larger males, where the size difference is greatest. It should also be noted that a significant interaction between sexes and localities in logCS and regression scores was detected in the lateral aspect of the cranium: while males are generally larger in *S. murinus*, a reversal is observed in western Myanmar (Fig. 4). This may indicate unique sexual differences in western Myanmar, such as the occipital height and sagittal crest development, which are only apparent in the lateral aspect of the cranium.

Adaptive significance of allometric shape changes

The positive regression scores on each aspect of the skull revealed specific allometric shape changes in larger individuals of *S. murinus*. These changes included a wider base of the upper and lower first incisor, a well-developed glenoid fossa, an anterior downward shift in the lateral projection of the maxilla, an anterior shift in the pterygoid hamulus, and a well-developed parietal bone (Figs. 2D, 3A and B). These

shape changes were found in the sites of attachment of muscles or tendons between the cranium and the mandible that are involved in feeding. Similar allometric shape changes in craniofacial bones with increasing body size are commonly observed in other mammals, including rodents and carnivores (Slater and Van Valkenburgh 2009; Gonzalez et al. 2013; Usui and Tokita 2018). On the other hand, in *S. murinus*, there were some unique allometric deviations from the common allometric trends seen in other mammals: development and the forward shift of the maxilla and the pterygoid hamulus (Figs. 2, 3A and B). Alternatively, it involves the elongation of the rostrum, the frontal bone, and the orbitotemporal fossa, coupled with the development of the parietal bone. These morphological trends are possibly related to specific physical characteristics of *S. murinus*, such as the lack of zygomatic arches and an "inflexible" mandible (functioning only in an up-and-down motion), which is a morphological feature specific to Eulipotyphla (Ôta et al. 1985). The development of the base of the first incisor in *S. murinus* is also notable. Several species of the genus Sorex, *S.*

araneus and *S. minutus*, are known to often use subterranean habitat during the winter season (Michielson 1966), and it may reflect an increase in feeding on earthworms (Hamilton 1930; Pernetta 1976; Abe 1985). Although *S. murinus* is not a subterranean species, a significant portion (25.4%) of the stomach contents in Himalayan *S. murinus* consisted of earthworms (Abe 1982). The well-developed incisors in larger *S. murinus* may play a crucial role in piecing or decaying soils and woods to access food resources such as earthworms.

Prospects for a morphological understanding of S. murinus *over the whole distribution*

This study elucidated the differences in skull morphology among the three lineages within Myanmar, and the geographically adjacent populations in Bangladesh and Vietnam. *Suncus murinus* has expanded its distribution widely to the Indian Ocean coast, including many small islands, and they are clustered within Lineage I along with Vietnamese population (Ohdachi et al. 2024). By referencing the morphological

characteristics revealed in this study, conducting additional morphometric analyses, including populations that have expanded with human activities, is expected to contribute to a more comprehensive morphological understanding of *S. murinus*.

Conclusion

Until now, considerable attention has been given to the intraspecific variation on body size of *S. murinus*. However, as body sizes overlap among lineages, the morphological differences between lineages have not been well understood. This study elucidated for the first time the differences in skull morphology among the three lineages within Myanmar, and the geographically adjacent populations in Bangladesh and Vietnam by investigating size allometric shape changes and non-allometric shape variations. While skull size and allometric shape changes suggested the presence of intermediate individuals among central Myanmar, southern Myanmar, and Vietnam populations, non-allometric shape variations clearly delineate differences among these populations. Additionally, allometric shape changes were observed in the sites of attachment of

muscles or tendons between the cranium and the mandible associated with piecing or decaying. Our findings provide fundamental insights into the skull morphological features of *S. murinus* and are expected to contribute to a more comprehensive understanding of the evolutionary processes of morphological variation in *S. murinus*.

Supplementary data

Supplementary Table S1. Definitions of 30 landmarks on the ventral aspect of the cranium, 14 landmarks and 8 semi-landmarks on the lateral aspect of the cranium, and 10 landmarks on the lateral aspect of the mandible examined in this study.

Acknowledgments: We are grateful to J. Shi for her preliminary analyzing. We express immense gratitude to two anonymous reviewers and the Associate Editor for critiques that significantly improved this manuscript. The present study was partly granted by

JSPS KAKENHI Grant-in-Aid for Scientific Research (B) Numbers JP25304009 and JP24404045.

References

Abe, H. 1982. Ecological distribution and faunal structure of small mammals in central Nepal. Mammalia 46: 477–503.

Abe, H. 1985. Classification, distribution and ecology of the Soricidae, considered from the standpoint of adaptive radiation. In (Kondo, K., Oda, S., Kitoh, J., Ôta, K. and Isomura, G., eds.) *Suncus murinus* Biology of the Laboratory Shrew, pp. 20–37. Japan Scientific Societies Press, Tokyo (in Japanese with English summary).

Adams, D., Collyer, M., Kaliontzopoulou, A. and Baken, E. 2023. "Geomorph: Software for geometric morphometric analyses. R package version 4.0.6."

Available at https://cran.r-project.org/package=geomorph (Accessed 25 January 2024).

Baken, E., Collyer, M., Kaliontzopoulou, A. and Adams, D. 2021. geomorph v4.0 and gmShiny: enhanced analytics and a new graphical interface for a comprehensive morphometric experience. Methods in Ecology and Evolution 12: 2355–2363.

Bergmann, C. 1847. Ueber die Verhältnisse der Wärme ökonomie der Thiere zu ihrer Grösse. Göttinger Studien 3: 595–708 (in German).

Blackburn, T. M., Gaston, K. J. and Loder, N. 1999. Geographic gradients in body size: a clarification of Bergmann's rule. Diversity and Distributions 5: 165–174.

Bookstein, F. L. 1991. Morphometric tools for landmark data: Geometry and biology. Cambridge University Press, Cambridge, 435 pp.

Burgin, C. J. and He, K. 2018. Family Soricidae (shrews). In (Wilson, D. E. and Mittermeier, R. A., eds.) Handbook of the Mammals of the World. Vol. 8. Insectivores, Sloths and Colugos, pp. 332–551. Lynx Edicions, Barcelona.

Collyer, M. and Adams, D. 2023. RRPP: Linear Model Evaluation with Randomized Residuals in a Permutation Procedure, R package version 1.4.0. Available at https://cran.r-project.org/package=RRPP (Accessed 25 January 2024).

Ebukuro, S. 2011. Characteristics of vomition of Suncus murinus and cultivation of strains. In (Isomura, G., Oda, S., Toya, K. and Miyaki, T., eds.) Biology of *Suncus murinus*, pp. 90–92. Japan Scientific Societies Press, Japan (in Japanese).

Emerson, S. B. and Bramble, D. M. 1993. Scaling, allometry, and skull design. In (Hanken, J. and Hall, B. K., eds.), The Skull. Vol. 3: Functional and Evolutionary Mechanisms, pp. 384–421. Chicago University Press, Chicago, USA.

Gonzalez, P. N., Kristensen, E., Morck, D. W., Boyd, S. and Hallgrímsson, B. 2013. Effects of growth hormone on the ontogenetic allometry of craniofacial bones. Evolution & Development 15: 133–145.

Hamilton, W. J. 1930. The food of the Soricidae. Journal of Mammalogy, 11: 26–39.

Hutterer, R. 2005. Order Soricomorpha. In (Don, E. W. and DeeAnn, M. R., eds.) Mammal Species of the World, A taxonomic and geographic reference 1, pp. 220–311. Johns Hopkins University Press, Baltimore.

Hutterer, R. and Trainer, M. 1990. The immigration of the Asian house shrew (*Suncus murinus*) into Africa and Madagascar. Vertebrates in the Tropics. Bonn: Museum Alexander Koenig. 309–319.

Ikeda, Y., Jiang, T., Oh, H., Csorba, G. and Motokawa, M. 2020. Geographic variations of skull morphology in *Rhinolophus ferrumequinum* species complex (Mammalia: Chiroptera). Zoologischer Anzeiger 288: 125–138.

Ishikawa, A. and Namikawa, T. 1987. Postnatal growth and development in laboratory strains of large and small musk shrews (*Suncus murinus*). Journal of Mammalogy 68: 766–774.

Ishikawa, A. and Namikawa, T. 1991. Postnatal growth pattern of F_1 hybrids of a cross between two strains of large and small musk shrews, *Suncus murinus*. Experimental Animals 40: 223–230.

Ishikawa, A., Yamagata, T. and Namikawa, T. 1995. Relationships between morphometric and mitochondrial DNA differentiation in laboratory strains of musk shrews (*Suncus murinus*). The Japanese Journal of Genetics 70: 57–74.

Klingenberg, C. P. 2011. MorphoJ: an integrated software package for geometric morphometrics. Molecular Ecology Resources 11: 353–357. Available at https://morphometrics.uk/MorphoJ_page.html (Accessed 25 January 2024).

Klingenberg, C. P. 2016. Size, shape, and form: concepts of allometry in geometric morphometrics. Development Genes and Evolution 226: 113–137.

Kurachi, M., Chau, B. L., Dang, V. B., Dorji, T., Yamamoto, Y., Nyunt, M. M., Maeda, Y., Chhum-Phith, L., Namikawa, T. and Yamagata, T. 2007a. Population structure of wild musk shrews (*Suncus murinus*) in Asia based on mitochondrial

DNA variation, with research in Cambodia and Bhutan. Biochemical Genetics 45: 165–183.

Kurachi, M., Kawamoto, Y., Tsubota, Y., Chau, B. L., Dang, V. B., Dorji, T., Yamamoto, Y., Nyunt, M. M., Maeda, Y., Chhum-Phith, L., et al. 2007b. Phylogeography of wild musk shrew (*Suncus murinus*) populations in Asia based on blood protein/enzyme variation. Biochemical Genetics 45: 543–563.

Marroig, G., Shirai, L. T., Porto, A., de Oliveira, F. B. and De Conto, V. 2009. The evolution of modularity in the mammalian skull II: Evolutionary consequences. Evolutionary Biology 36: 136–148.

Michielson, N. C. 1966. Intraspecific and interspecific competition in the shrews *Sorex Araneus L.* and *S. minutus L.* Archives Néerlandaises de Zoologie 17: 73–174.

Motokawa, M. 2015. *Suncus murinus* (Linnaeus, 1766). In (Ohdachi, S. D., Ishibashi, Y., Iwasa, M. A., Fukui, D. and Saitoh, T., eds.) The Wild mammals in Japan, Second edition, pp. 26–27. Shoukadoh, Kyoto.

Oda, S. and Kondo, K. 1976. Progress in domestication of *Suncus murinus riukiuanus* for experiments. Mammalian Sciences 33: 13–30 (in Japanese).

Ohdachi, S. D. 2021. Phylogeography of shrews –repeated migrations by human. Biostory 36: 24–33. (in Japanese).

Ohdachi, S. D., Fujiwara K., Shekhar, C., Son, N. T., Suzuki, H. and Osada, N. 2024. Phylogenetics and population genetics of the Asian house shrew *Suncus murinus*–*S. montanus* species complex inferred from whole-genome and mitochondrial DNA sequences, with special reference to the Ryukyu Archipelago, Japan. Zoological Science 41: 216–229.

Ohdachi, S. D., Kinoshita, G., Nasher, A. K., Yonezawa, T., Arai, S., Kikuchi, F., Kyaw San, L. and Saw, B. 2017. Re-evaluation of the phylogeny based on mitochondrial cytochrome *b* gene in the house shrew, *Suncus murinus*-*S. montanus* species complex, with special reference to Yemen and Myanmar populations. Journal of Wildlife and Biodiversity 1: 79–87.

Ohdachi, S. D., Kinoshita, G., Oda, S. I., Motokawa, M., Jogahara, T., Arai, S., Nguyen, S. T., Suzuki, H., Katakura, K., Bawm, S., et al. 2016. Intraspecific phylogeny of the house shrews, *Suncus murinus*-*S. montanus* species complex, based on the mitochondrial cytochrome *b* gene. Mammal Study 41: 229–238.

Ôta, K., Kitoh, J. and Isomura, G. 1985. Ⅳ. Anatomy and histology of the house musk shrew. 2. Skeletal system. In (Kondo, K., Oda, S., Kitoh, J., Ôta, K. and Isomura, G., eds.) *Suncus murinus* biology of the laboratory shrew, pp. 185–198. Japan Scientific Societies Press, Tokyo (in Japanese).

Pernetta, J. C. 1976. Diets of the shrews *Sorex Araneus L*. and *Sorex minutus L*. in Wytham grassland. Journal of Animal Ecology 45: 889–912.

R Development Core Team. 2022. R for Windows, Version 4.2.2. R Foundation for Statistical Computing, Vienna. Available at http://www.R–project.org (Accessed 30 March 2023).

Rohlf, F. J. 2017. TpsDig, version 2.31. Ecology and evolution and anthropology. Stony Brook University, New York. Available at https://sbmorphometrics.org/ (Accessed 21 March 2024).

Rohlf, F. J. 2018. Tps utility program, version 1.78. Ecology and evolution and anthropology. Stony Brook University, New York. Available at https://sbmorphometrics.org/ (Accessed 21 March 2024).

Rohlf, F. J. and Slice, D. 1990. Extractions of the Procrustes method for the optimal superimposition of landmarks. Systematic Biology 39: 835–844.

Slater G. J. and Van Valkenburgh B. 2009. Allometry and performance: the evolution of skull form and function in felids. Journal of Evolutionary Biology 22: 2278–2287.

Usui, K. and Tokita, M. 2018. Creating diversity in mammalian facial morphology: a review of potential developmental mechanisms. Evo Devo 9: 1–17.

Yamagata, T. 2011. Genetic differentiation of wild musk shrew populations in Asia based on mitochondrial DNA and blood protein/enzyme variations. In (Isomura, G., Oda, S., Toya, K. and Miyaki, T., eds.) Biology of *Suncus murinus*, pp. 285–290. Japan Scientific Societies Press, Japan (in Japanese).

Yamagata, T., Ohishi, K., Faruque, M. O., Masangkay, J. S., Ba-Loc, C., Vu-Binh, D., Mansjoer, S. S., Ikeda, H. and Namikawa, T. 1995. Genetic variation and geographic distribution on the mitochondrial DNA in local populations of the musk shrew, *Suncus murinus*. The Japanese Journal of Genetics 70: 321–337.

Yoshida, T. H. 1982. Cytogenetical studies on Insectivora. The Japanese Journal of Genetics 57: 101–111.

Figure legends

Fig. 1. The locality map used in this study. The symbols represented in left lower legends are corresponded with each locality. The detailed information about locality

name and sex is available at the link below:

https://www.google.com/maps/d/edit?mid=1JvPgDIEzyaMAQHqGWVmcPLEPCbijRWo&usp=sharing.

Fig. 2. Landmarks used in geometric morphometrics in this study. A, 30 landmarks on the ventral aspect of the cranium. B, 14 landmarks (dots) and 8 semi-landmarks (squares) on the lateral aspect of the cranium. C, 10 landmarks on the lateral aspect of the mandible. D, the mean transformation grid of the ventral aspect of the cranium (upper), the lateral aspect of the cranium (middle), and the lateral aspect of the mandible (bottom). The definitions for each landmark were represented in Table S1.

Fig. 3. Scatter plots of the logged centroid size and regression score of the ventral aspect of the cranium (A), the lateral aspect of the cranium (B), and the lateral aspect of the mandible (C). Symbols legend corresponding to the localities were represented on A. Positive transformation grids were represented on upper right, and negative

transformation grids were on lower left, respectively. 95% confidence intervals were shaded along each regression line.

Fig. 4. Boxplots of the logged centroid size (left) and regression score (right) of the ventral aspect of the cranium (A), the lateral aspect of the cranium (B), and the lateral aspect of the mandible (C). Boxplots were represented by localities and sexes (females are left [red] and males are right [blue]) separately. The combinations of the lowercase alphabets above each boxplot were represented the results of Tukey HSD. The abbreviations: Ban, Bangladesh; W Mya, western Myanmar; C Mya, central Myanmar; S Mya, southern Myanmar; Viet, Vietnam.

Fig. 5. Scatter plots of the canonical variate 1 and 2 of the ventral aspect of the cranium (A), the lateral aspect of the cranium (B), and the lateral aspect of the mandible (C). Symbols legend corresponding to the localities were represented on A. Positive and negative transformation grids were represented along each axis, respectively. 95% confidence ellipses were shaded around each plot.

Fig. 6. Scatter plots of the canonical variate 3 and 4 of the ventral aspect of the cranium (A), the lateral aspect of the cranium (B), and the lateral aspect of the mandible (C). Symbols legend corresponding to the localities were represented on A. Positive and negative transformation grids were represented along each axis, respectively. 95% confidence ellipses were shaded around each plot.

Appendix 1. Scatter plots of the logged centroid size and body weight of the ventral aspect of the cranium (A), the lateral aspect of the cranium (B), and the lateral aspect of the mandible (C). Symbols legend corresponding to the localities were represented on A. Pearson correlation coefficient (*r*) were represented on upper left, respectively. 95% confidence intervals were shaded along each regression line.

Table 1. Specimen list examined in this study. Avairable at the link below:
https://www.google.com/maps/d/edit?mid=1JvPgDIEzyaMAQHqGWVmcPLEPCbijRWo&usp=sharing

Locality	Sample size	
	Male	Female
Bangladesh	10	12
W. Myanmar	3	5
C. Myanmar	6	5
S. Myanmar	22	27
Vietnam	19	18

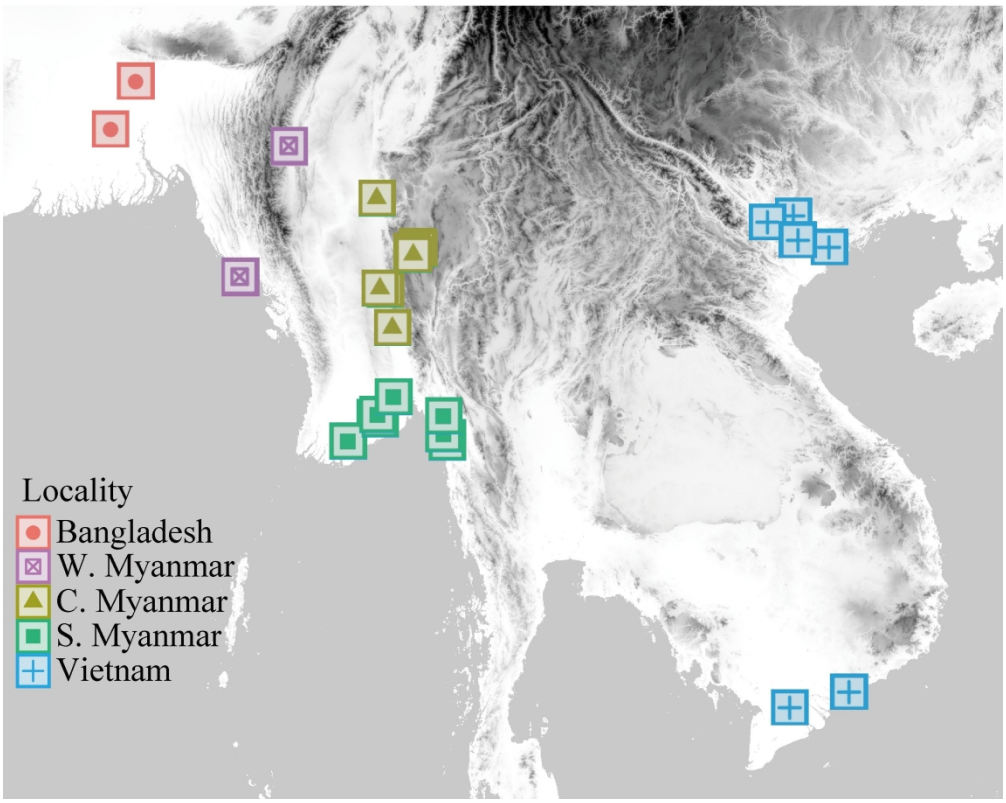

Fig. 1. The locality map used in this study. The symbols represented in left lower legends are corresponded with each locality. The detailed information about locality name and sex is available at the link below: https://www.google.com/maps/d/edit?mid=1JvPgDIEzyaMAQHqGWVmcPLEPCbijRWo&usp=sharing.

125x99mm (600 x 600 DPI)

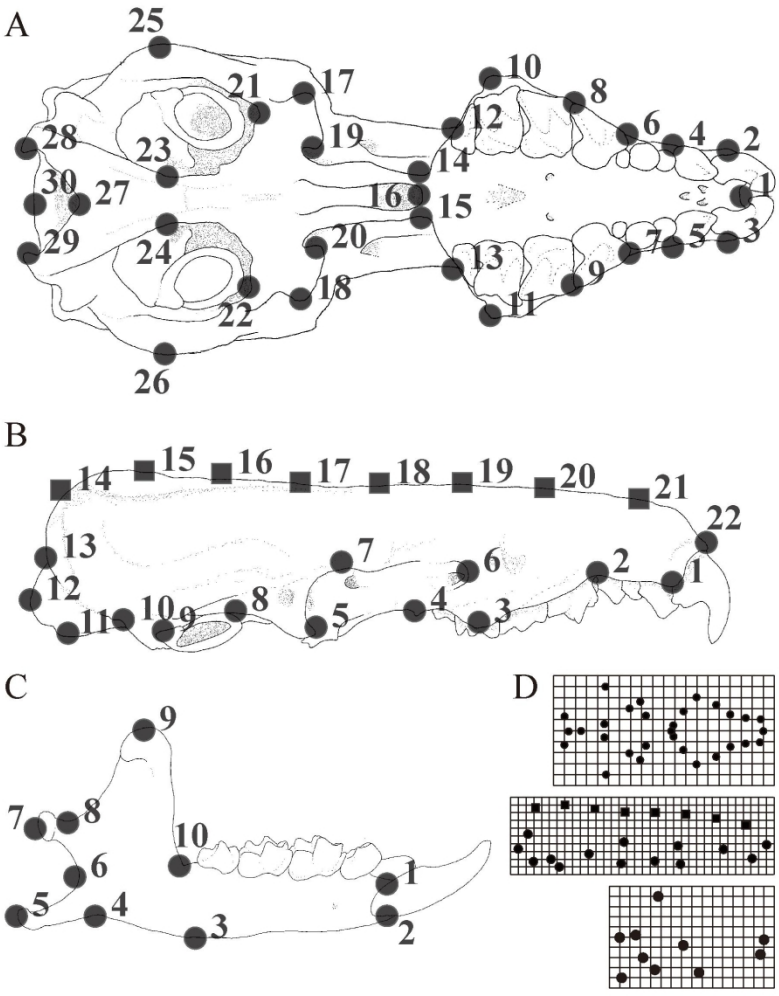

Fig. 2. Landmarks used in geometric morphometrics in this study. A, 30 landmarks on the ventral aspect of the cranium. B, 14 landmarks (dots) and 8 semi-landmarks (squares) on the lateral aspect of the cranium. C, 10 landmarks on the lateral aspect of the mandible. D, the mean transformation grid of the ventral aspect of the cranium (upper), the lateral aspect of the cranium (middle), and the lateral aspect of the mandible (bottom). The definitions for each landmark were represented in Table S1.

97x117mm (600 x 600 DPI)

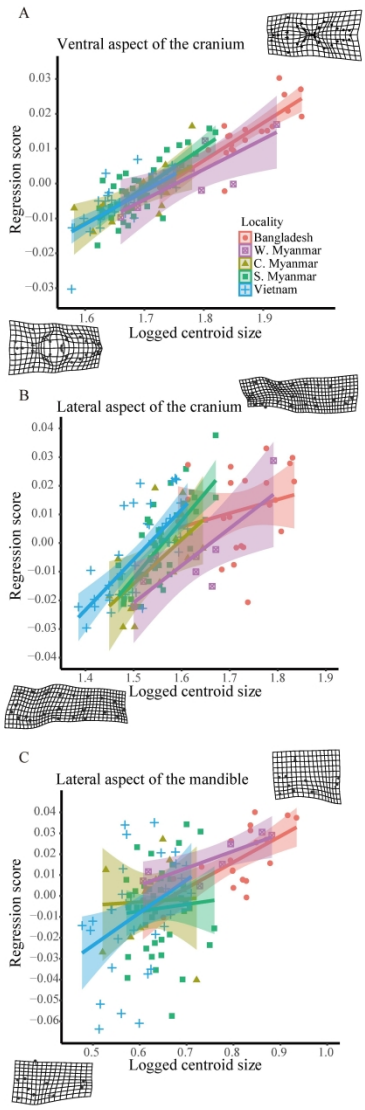

Fig. 3. Scatter plots of the logged centroid size and regression score of the ventral aspect of the cranium (A), the lateral aspect of the cranium (B), and the lateral aspect of the mandible (C). Symbols legend corresponding to the localities were represented on A. Positive transformation grids were represented on upper right, and negative transformation grids were on lower left, respectively. 95% confidence intervals were shaded along each regression line.

97x264mm (600 x 600 DPI)

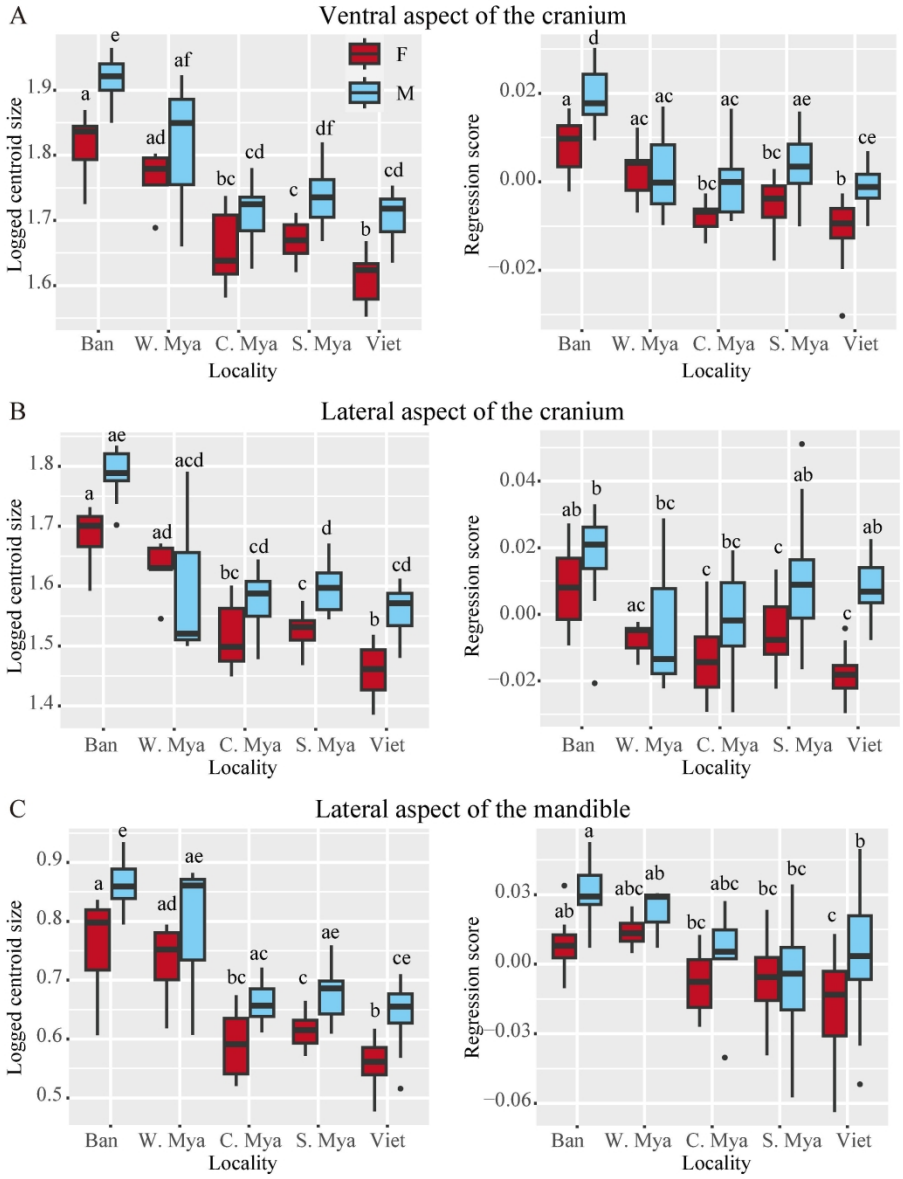

Fig. 4. Boxplots of the logged centroid size (left) and regression score (right) of the ventral aspect of the cranium (A), the lateral aspect of the cranium (B), and the lateral aspect of the mandible (C). Boxplots were represented by localities and sexes (females are left and males are right) separately. The combinations of the lowercase alphabets above each boxplot were represented the results of Tukey HSD. The abbreviations: Ban, Bangladesh; W Mya, western Myanmar; C Mya, central Myanmar; S Mya, southern Myanmar; Viet, Vietnam.

125x162mm (600 x 600 DPI)

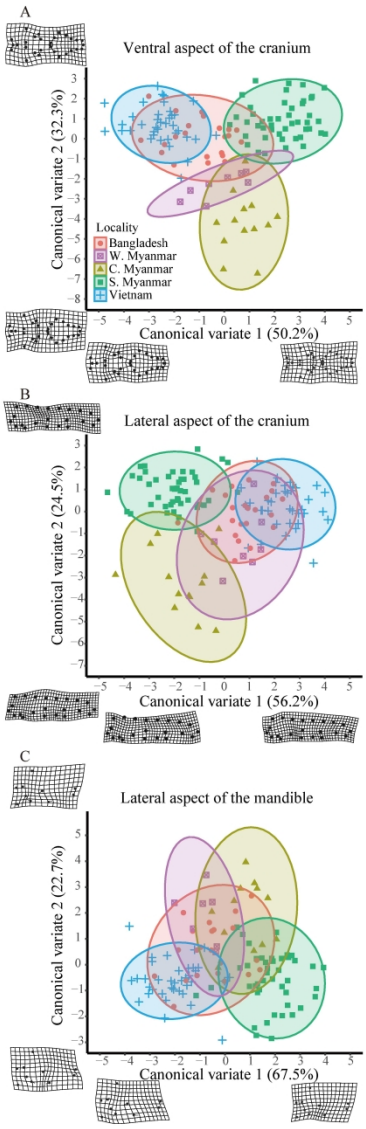

Fig. 5. Scatter plots of the canonical variate 1 and 2 of the ventral aspect of the cranium (A), the lateral aspect of the cranium (B), and the lateral aspect of the mandible (C). Symbols legend corresponding to the localities were represented on A. Positive and negative transformation grids were represented along each axis, respectively. 95% confidence ellipses were shaded around each plot.

97x264mm (600 x 600 DPI)

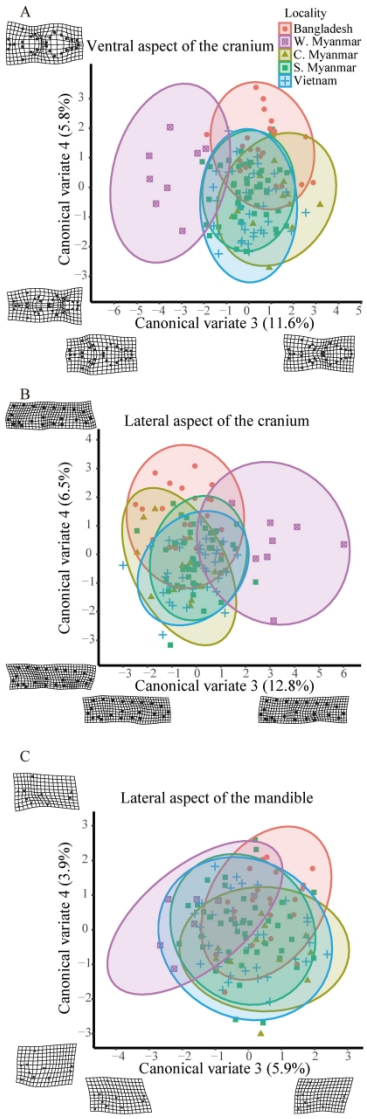

Fig. 6. Scatter plots of the canonical variate 3 and 4 of the ventral aspect of the cranium (A), the lateral aspect of the cranium (B), and the lateral aspect of the mandible (C). Symbols legend corresponding to the localities were represented on A. Positive and negative transformation grids were represented along each axis, respectively. 95% confidence ellipses were shaded around each plot.

97x264mm (600 x 600 DPI)

Table: Definitions of 30 landmarks
cranium, and 10 landmarks on the l

Direction	Landmark No.
Ventral cranium	1
	2
	3
	4
	5
	6
	7
	8
	9
	10
	11
	12
	13
	14
	15
	16
	17
	18
	19
	20
	21
	22
	23
	24
	25
	26
	27
	28
	29
	30
Leteral cranium	1
	2
	3
	4
	5
	6
	7
	8
	9
	10
	11
	12
	13
	14-21
	22
Lateral mandible	1

2
3
4
5
6
7
8
9
10

; on the ventral aspect of the cranium, 14 landmarks and 8 semi-landmarks on the lateral aspect of the lateral aspect of the mandible examined in this study

Definition
Anterior point of the midline suture between the premaxillae
Outer basal of the first incisor (R)
Outer basal of the first incisor (L)
Posterior outer basal of the second incisor (R)
Posterior outer basal of the second incisor (L)
Anterior outer basal of the fourth premolar (R)
Anterior outer basal of the fourth premolar (L)
Anterior outer basal of the first molar (R)
Anterior outer basal of the first molar (L)
Lateral margin of the maxilla (R)
Lateral margin of the maxilla (L)
Intersection between the anterior margin of the fossa orbitotemporalis and the maxilla (R)
Intersection between the anterior margin of the fossa orbitotemporalis and the maxilla (L)
Intersection between the lateral margin of the pterygoid plates and the posterior margin of the palate (R)
Intersection between the lateral margin of the pterygoid plates and the posterior margin of the palate (L)
Midline of the posterior margin of the palate
Distal margin of the glenoid fossa (R)
Distal margin of the glenoid fossa (L)
Proximal margin of the glenoid fossa (R)
Proximal margin of the glenoid fossa (L)
Anterior margin of the tympanic cavity space (R)
Anterior margin of the tympanic cavity space (L)
Proximal margin of the basilar part of the occipital bone (R)
Proximal margin of the basilar part of the occipital bone (L)
Distal margin of the mastoid process (R)
Distal margin of the mastoid process (L)
Midline of the anterior margin of the foramen magnum
Medial end of the posterior margin of the occipital condyle (R)
Medial end of the posterior margin of the occipital condyle (L)
Posterior margin of the occipit
Posterior basal margin of the first incisor
Basal margin of the canine
Outer margin of the maxilla
Outer margin of the palate
Anterior margin of the pterygoid hamulus
Anterior margin of the pterygopalatine fossa
Intersection between the posterior frontal bone and the anterior temporalis crest
Dorsal margin of the posterior temporalis crest
Anterior basal margin of the petrous part of the temporal bone
Posterior basal margin of the petrous part of the temporal bone
Ventral margin of the occipital condyle
Posterior margin of the occipital condyle
Dorsal margin of the occipital condyle
Equidistant between landmarks 13 and 22, following the sagittal crest contour
Anterior basal margin of the first incisor
Dorsal basal margin of the first incisor

Ventral basal margin of the first incisor
Bottom of the posterior convex saddle of the body of the mandible
Inferior side of the junction of the angular process to the body of the mandible
Posterior end of the angular process
Superior side of the junction of the angular process to the body of the mandible
Posterior end of the dorsal facet of the condyle
Inferior point of the saddle between the condylar and coronoid processes
Dorsal end of the superior crest of the coronoid process
The junction of the ramus and the body of the mandible

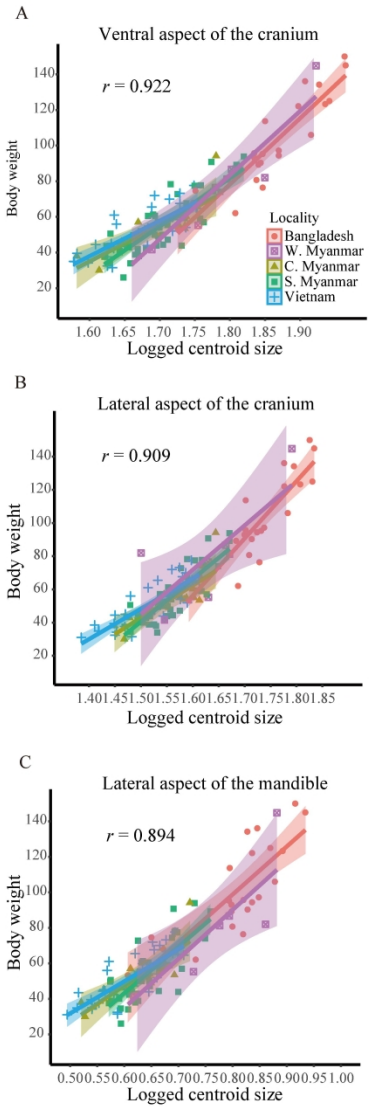

90x226mm (600 x 600 DPI)